Ultralow lattice thermal conductivity in complex structure $Cu_{26}V_2Sn_6Se_{32}$ due to interaction of low-frequency acoustic-optical phonons

Kewal Singh Rana [1], Debattam Sarkar,[2] Nidhi,[3] Aditya Singh [1], Chandan Bera,[3] Kanishka Biswas,[2] and Ajay Soni [1,*]

[1]*School of Physical Sciences, Indian Institute of Technology Mandi, Mandi 175075, Himachal Pradesh, India*

[2]*New Chemistry Unit, School of Advanced Materials and International Centre of Materials Science, Jawaharlal Nehru Centre for Advanced Scientific Research (JNCASR), Jakkur, Bangalore 560064, India*

[3]*Institute of Nano Science and Technology, Knowledge City, Sahibzada Ajit Singh Nagar, 140306 Punjab, India*

Damping of phonon momentum suppresses the lattice thermal conductivity (κ_1) through low-energy acoustic-optical phonon interactions. We studied the thermal transport properties and underlying mechanism of phonon interactions in the large unit cell $Cu_{26}V_2Sn_6Se_{32}$. The large number of atoms in the unit cell results in low acoustic phonon cutoff frequency, flat phonon branches, low-frequency Raman active modes, localized rattlerlike vibrations and strong crystalline anharmonicity. The crystal structure complexity disrupts the phonon propagation through weak bonded Cu atoms, bosonlike peak and poor phonon velocity. The sulfur at selenium sites ($Cu_{26}V_2Sn_6Se_{30}S_2$) distort the crystal lattice by offering additional scattering mechanism at the anionic sites, thereby increasing the power factor and decreasing the κ_1. This strategic manipulation of phonon scattering towards ultralow κ_1 not only results in improved thermoelectric performance but also offers insights into the fundamental understanding of heat transport in complex structured, large unit cell compounds.

I. INTRODUCTION

Complex large unit cell minerals have been studied widely in the fields of thermoelectric (TE), thermal barrier coating, and thermal management in electronic devices, because of inherent low lattice thermal conductivity (κ_1) [1–4]. Due to abundance, ecofriendliness, and absence of rare-earth elements (such as Bi, Sb, Pb, Cd and Te), minerals can be future candidates for green energy harvesting technologies [1–3]. In this regard, it is pivotal to demonstrate the fundamental understanding of poor thermal transport of complex crystal structured minerals where the enhanced phonon scattering is an essential requirement [5–7].

The inherently low κ_1 in minerals is mainly arising from large number of unit cell atoms [5,8], robust acoustic-optical phonon interactions [5,9], soft chemical bonding [10], rattlinglike localized vibrations [5,10], crystal defects and disorders [1,11]. According to kinetic theory and Boltzmann transport equation: $\kappa_1 = \frac{1}{3}(C_v \, v \, l)$, where C_v is the heat capacity, v is the phonon group velocity, and l is the phonon mean-free path [7]. For C_v, the large number of unit cell atoms (n) results in ($3n$) vibrational modes strongly hinders the momentum of phonons through strong acoustic-optical phonon interactions [5–7]. The presence of heavy atoms, weak chemical bonding, low elastic modulus altogether lowers the phonons group velocity (v) [7]. While, the presence of grain boundaries, crystal defects, disorders, and nanostructuring lowers the mean-free path of phonon (l) through multiple phonon scattering channels [1,7,11,12].

In TEs, generally, the large unit cell minerals are transition-metal (Fe, Mn, Zn, Co, Cr, Nb, V, Ni)-based ternary and quaternary chalcogenides, which have shown the greatest impact in the community recently due to inherent low κ_1 values [2,4,5]. The minerals such as colusites [1,11,13], tetrahedrites [14,15], argyrodites [8], chalcopyrites [16], sulfide bornite [17], kuramite [18], kesterite [19], and Cu_3BiS_3 [20] belong to the family of large unit cell or the complex crystal structure compounds. The poor thermal properties in these compounds generally arise due to rattlinglike vibrations at low frequency, large average Grüneisen parameter, soft chemical bonding, and poor sound propagation, which altogether arise from Cu atoms bonding [20,21]. The bonding of Cu atoms majorly defines the lattice dynamics, where the asymmetric or weakly coordinated specific Cu atoms enhances the crystal anharmonicity [20–22]. Colusite is one such mineral where the large number of atoms per unit cell results in extremely low κ_1 via structural complexity, strong crystal anharmonicity, soft Cu-S crystal framework, and strong acoustic-optical phonon interaction [1]. The excess negative charge in ions, $(Cu_{26})^+$, $(V_2)^{5+}$, $(Sn_6)^{4+}$, and $(S_{32})^{2-}$ results in electron-deficient character, and shows the heavily degenerate p-type semiconducting behavior [23]. The sulfur sublimation in colusite brings the atomic-scale defects resulting in disordered phase and enhanced phonon scattering [11,24]. Currently, the optimized doping and substitution concentrations at the cationic sites results in saturation of κ_1 values (~ 0.4 W/mK) [1,9]. Hence, the replacement of sulfur at anionic site with heavy selenium can be an effective route to study the thermal properties due to modified chemical bonding and lattice dynamics. Tailoring at the anion sites with different compositions can also make a better TE material through providing a

---

*Corresponding author: ajay@iitmandi.ac.in

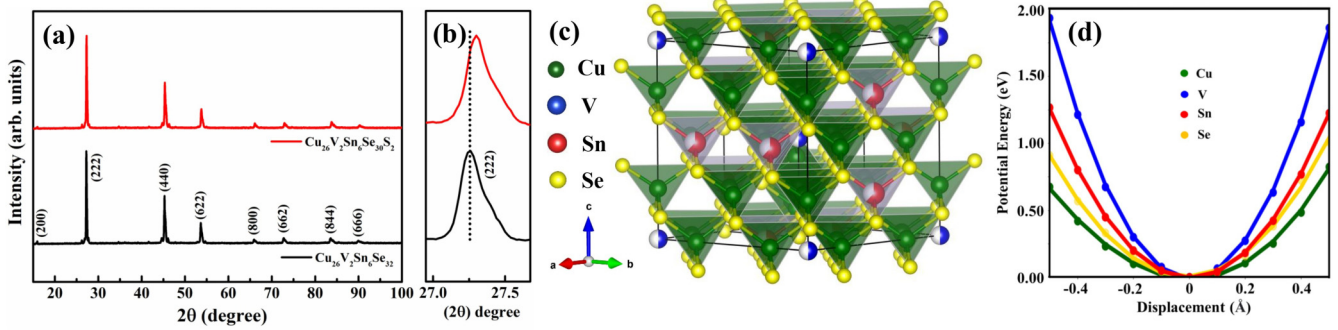FIG. 1. Powder XRD patterns of (a) CVS$-$Se$_{32}$ and CVS$-$Se$_{30}$S$_2$, (b) the enlarged (222) reflection showing the right shift in CVS$-$Se$_{30}$S$_2$ with respect to CVS$-$Se$_{32}$, (c) the cubic polyhedral structure of CVS$-$Se$_{32}$, and (d) potential energy vs relative movement of all elements representing the relatively rigid nature of V and Sn cations with respect to soft bonded Cu cations.

clean pathway for electrical transport and distorted channels for phonon propagation.

The current study explores the poor thermal transport properties in large unit cell synthetic Cu$_{26}$V$_2$Sn$_6$Se$_{32}$ (CVS$-$Se$_{32}$) and sulfur-doped Cu$_{26}$V$_2$Sn$_6$Se$_{30}$S$_2$ (CVS$-$Se$_{30}$S$_2$) materials. In CVS$-$Se$_{30}$S$_2$, the poor average sound velocity and large Grüneisen parameter reveal the presence of crystalline anharmonicity. The large number of primitive unit cell atoms strongly hinders the efficiency of heat carrying acoustic phonons through low acoustic phonon cutoff frequency. The low-frequency optical phonons strongly interact with acoustic phonons and boosts the scattering mechanism. The presence of bosonlike peak and existence of localized Einstein vibrational modes suggest the presence of disorder and triggers the multiphonon scattering processes. In comparison with earlier report of niobium (Nb)-based compounds, we observed relatively low electrical conductivity, high Seebeck coefficient, and optimized (low) charge carrier concentrations in vanadium (V)-based series of compounds. The variation in the physical properties is because of the difference of the atomic sizes of Nb ($\sim$1.46 Å) and V ($\sim$1.34 Å) and the electronegativity of chalcogens [9]. Among all the cations, the thermal and vibrational properties are mainly delivered by the weakly bonded Cu ions. The experimental studies are supported by the first-principles calculations through the electronic and phononic dispersion curves and density of states.

II. EXPERIMENTAL AND COMPUTATIONAL DETAILS

The polycrystalline samples Cu$_{26}$V$_2$Sn$_6$Se$_{32}$ and Cu$_{26}$V$_2$Sn$_6$Se$_{30}$S$_2$ were synthesized through the solid-state melting route. High-purity ($\sim$99.99%) raw elements (Cu, V, Sn, Se, and S) were weighed in stoichiometric amount and placed in clean quartz ampoules. The flame-sealed quartz ampules ($\sim$10^{-5} mbar) were slowly heated up to $\sim$1323 K and kept for 48 h and cooled down to room temperature [9]. Moreover, the synthesis of mixed chalcogen compounds (S over Se) is challenging due to low solubility limit (generally $\leqslant$10%) and high chances of getting secondary phases [25–27]. The obtained ingots were grounded into fine powder and subjected to spark plasma sintering (SPS) process to consolidate the sample for a period of $\sim$10 minutes at $\sim$773 K under a uniaxial pressure of $\sim$30 MPa and vacuum $\sim$10^{-3}

mbar. The density (d_m) of obtained SPS-processed coins were found to be $\sim$5.50 g cm^{-3} for both materials.

The phase purity and crystal structure were carried out through x-ray diffraction (XRD) obtained from rotating anode Rigaku Smart lab diffractometer and Cu$-$K$_\alpha$ radiation (wavelength $\sim$1.5406 Å). The field emission scanning electron microscopy (FE-SEM) images and elemental mapping were collected through JFEI, USA, Nova Nano SEM-450. The Raman spectroscopic measurements were carried out through Horiba Jobin-Yvon LabRAM HR evolution, 532 nm excitation laser, and 1800 grooves/mm grating. The ultralow frequency filters were used to identify the low-frequency modes. The temperature-dependent (300–773 K) electrical conductivity (σ) and Seebeck coefficient (S) measurements were performed using ZEM-3 (ULVAC-RIKO) on bar-shaped pellets under helium atmosphere. The charge carrier concentration and low-temperature C_p (specific heat) experiments were carried out through physical property measurement system (PPMS, Quantum Design). The total thermal conductivity (κ_{total}) was estimated using, $\kappa_{\text{total}} = DC_p d_m$, where D is the diffusivity. Further, the laser flash analysis (LFA) was used to measure D under a nitrogen atmosphere through Netzsch LFA-457, and C_p was estimated through the Dulong-Petit approximation. The longitudinal (ν_l) and transverse (ν_t) sound velocities were measured on the disc-shaped SPS-processed samples through an Epoch 650 Ultrasonic Flaw Detector (Olympus) having the transducer frequency 5 MHz.

Theoretical calculations were done inside the framework of density functional theory (DFT), the electronic structure was investigated within the Vienna *ab initio* Simulation Package (VASP) [28,29]. The kinetic cutoff energy of 420 eV was used to expand the wave function in basis set of plane waves in projected augmented wave (PAW) method, and Perdew-Burke-Ernzerhof (PBE) exchange correlation was applied. [28,30,31]. In combination with above a k mesh of $4 \times 4 \times 4$ was sampled in the reciprocal space. The convergence criterion of total energy was set to 10^{-8} eV and full optimization of structures was done until the force on each atom is 0.05 eV Å^{-1}. The crystal structure was relaxed to cubic crystal structure and space group symmetry P$\bar{4}$3n with lattice parameters, a $\sim$11.3136 Å and $\sim$11.3064 Å for CVS$-$Se$_{32}$ and CVS$-$Se$_{30}$S$_2$, respectively. Furthermore, PHONOPY software was used to calculate the phonon dispersion curve and a supercell of size $1 \times 1 \times 1$ and $1 \times 1 \times 1$ k points was considered for both the structures [32].
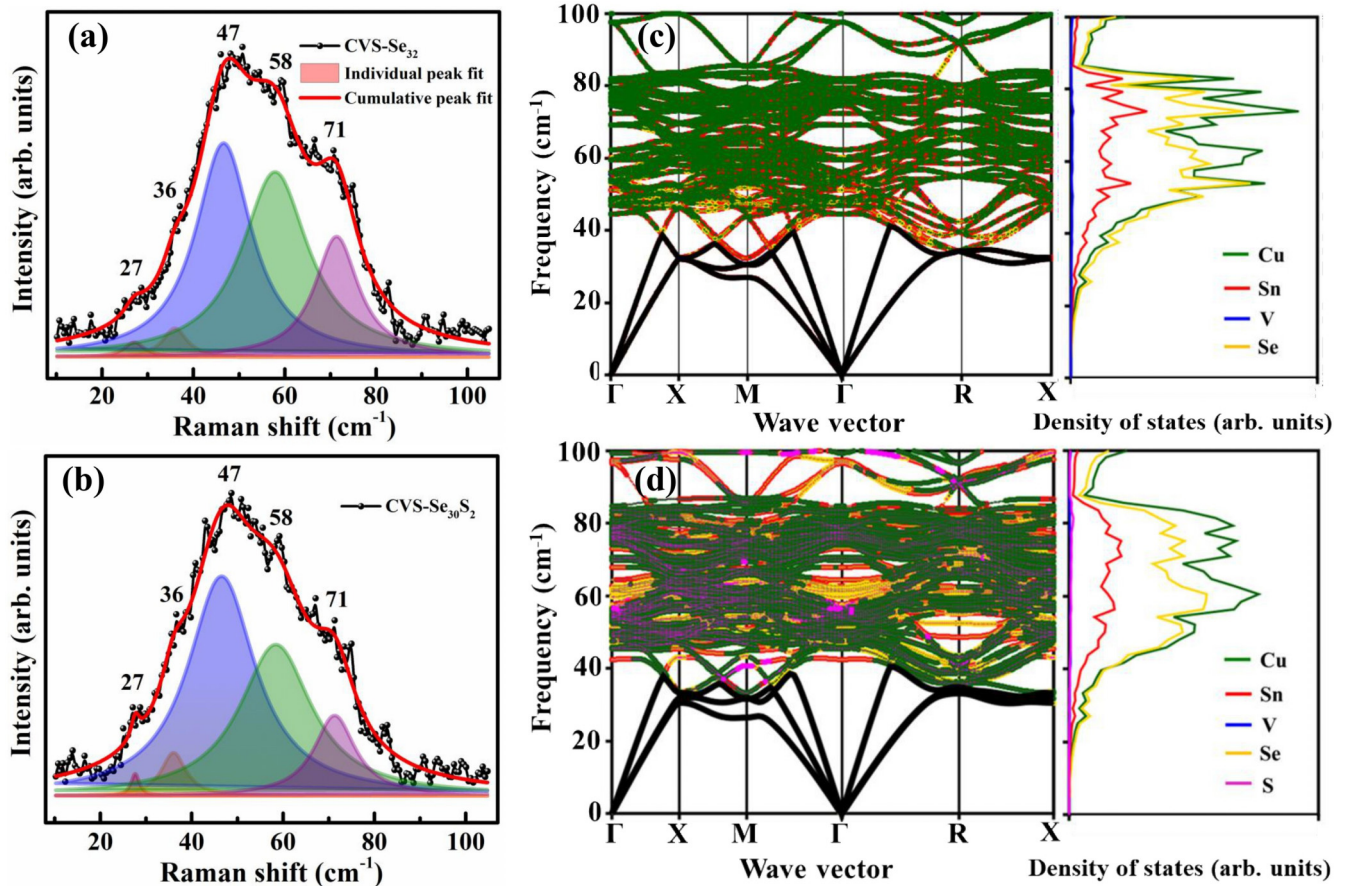
FIG. 2. (a), (b) Room temperature Raman spectra. (c), (d) Phonon dispersion curve and corresponding atom projected density of states for $CVS-Se_{32}$ and $CVS-Se_{30}S_2$, respectively.

III. RESULT AND DISCUSSION

A. X-ray diffraction

Figure 1(a) shows the XRD patterns of finely ground powder samples of $CVS-Se_{32}$ and $CVS-Se_{30}S_2$. Most of reflections are matching with earlier results of colusites having space group P$\bar{4}$3n and cubic crystal structure [1]. However, few reflections with very weak intensity ($\sim$26.2, 34.7, and 41.6°) refers the presence of secondary phases (Cu and Se phases). Due to complexity in the material system and synthesis process, minor compositions of secondary phases ($\sim$2%) are present. Regardless the synthesis procedure, the presence of secondary phases are common in these large unit cell complex structure compounds with V and Sn are the common cations, and offers negligible contributions to TE properties [1,33,34]. The Rietveld refined XRD pattern is shown in Fig. S1 of Supplemental Material (SM) [35], having refined lattice parameters ($a = b = c$) $\sim$11.3155 Å and unit cell volume (V_c)$\sim$1448.84 Å^3 for cubic $CVS-Se_{32}$. Further, the right shift of (222) diffraction peak of $CVS-Se_{30}S_2$ with respect to $CVS-Se_{32}$ [Fig. 1(b)] represents the lattice contraction ($a \sim$ 11. 2881 Å and $V_c \sim$ 1438.34 Å^3) due to lower radii sulfur in selenium sites. In comparison with earlier study of $Cu_{26}V_2Sn_6S_{32}$ colusite, the larger radii Se atom enhances V_c in $Cu_{26}V_2Sn_6Se_{32}$ by a factor of $\sim$15%, signifying the enhanced unit cell dimensions [36]. The cubic crystal structure of $CVS-Se_{32}$ is shown in Fig. 1(c) with five cationic sites, Cu

atom occupies 12f, 8e, and 6d, V occupies 2a and Sn occupies 6c atom; and Se atom occupies two anionic sites at 24i and 8e. All cations are tetrahedrally coordinated with Se anion and construct a large three-dimensional (Cu/V/Sn)$-$Se$_4$ network structure having 66 atoms in the primitive unit cell [1]. The microstructural FE-SEM images and elemental color mapping (Fig. S2, SM [35]) on clean and polished surface verifies the homogeneity and the uniform distribution of all the constituent elements. Furthermore, among all the cations, the shallow potential well of Cu atoms compared to Sn and V atoms shows the presence of soft or weak chemical bonding [Fig. 1(d)]. A small perturbation or thermal excitation is sufficient to disturb the Cu atoms from their equilibrium positions. The deeper potential energy well for Sn and V atoms shows the presence of rigidity in the crystal lattice. In this regard, the effect of Cu disturbance can play a vital role towards the thermal and vibrational properties of these materials.

B. Raman measurements

Figures 2(a) and 2(b) represent the Raman spectra of $CVS-Se_{32}$ and $CVS-Se_{30}S_2$ in the low-frequency regimes where the acoustic-optical phonon interactions play significant role towards thermal transport. Structurally, the large unit cell compounds with 66 atoms in the unit cell (n) results in maximum 195 (3n-3) optical modes with A$_1$, E, T$_1$,
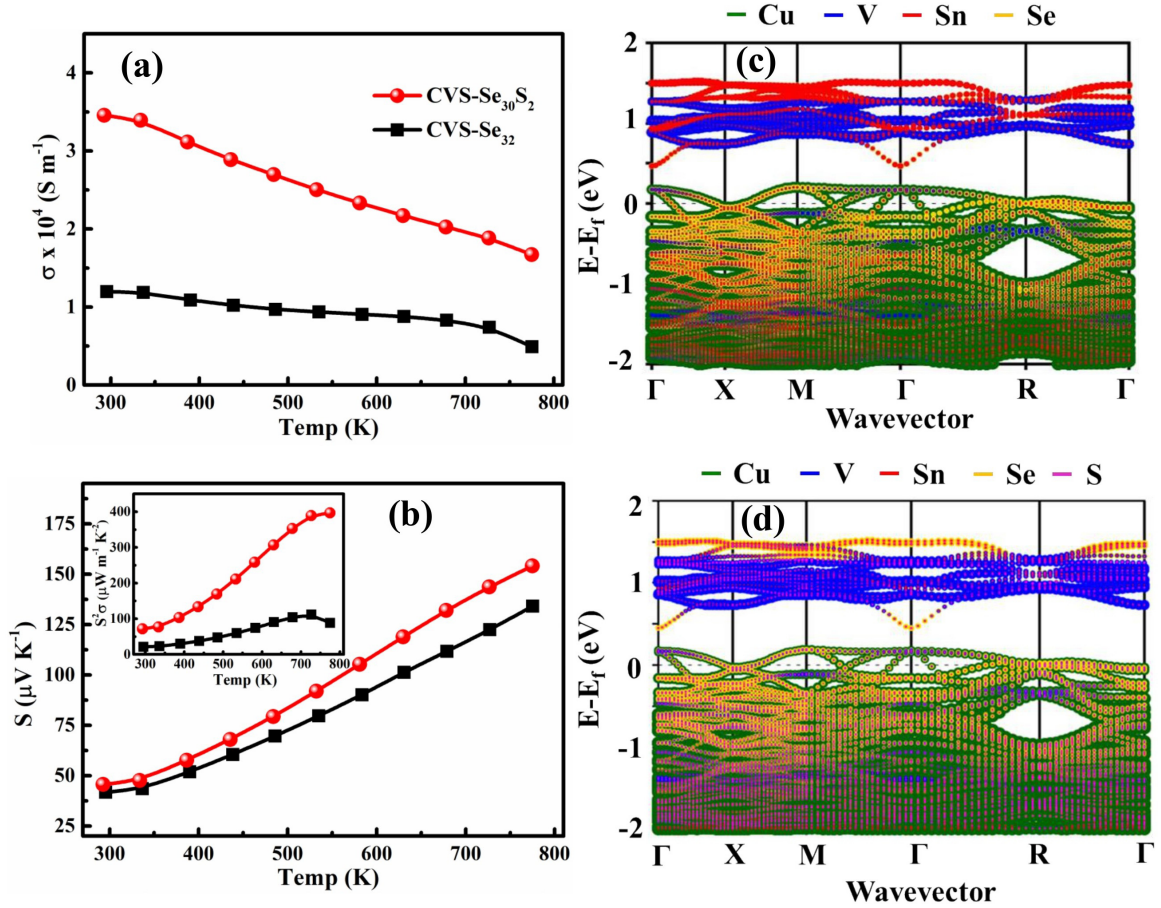
FIG. 3. Temperature-dependent (a) electrical conductivity, σ, (b) Seebeck coefficient, S, inset represents the power factor, $S^2\sigma$, and (c), (d) electronic dispersion curve for CVS$-$Se$_{32}$ and CVS$-$Se$_{30}$S$_2$, respectively.

and T$_2$ possible Raman mode symmetries. We have observed five low-frequency Raman active modes (below 100 cm^{-1}) for both materials, positioned at $\sim$27, 36, 47 (T$_1$), 58 (T$_1$), and 71 cm^{-1} (A$_2$). The phonon dispersion curve [Fig. 2(c)] shows the flat and compressed optical modes from $\sim$40 to $\sim$80 cm^{-1}, mainly associated with the vibration of soft bonded Cu atoms. The Cu cations are strongly vibrating relatively among all the cations as evident from the atom projected density of state calculations [Fig. 2(c)]. The eigen-vector visualization of Raman active modes are shown in Fig. S3, SM [35]. At X, M, and R symmetry points, the lowest possible optical phonon modes are observed [Fig. 2(c)] and the eigenvector visualization are shown in Fig. S4, SM [35]. The interaction of these modes with heat carrying acoustic branches changes the phonon's momentum. The sulfur incor-poration provides the disorder in the anionic sites of crystal lattice, which reduces the overall stiffness of the lattice and decreases the effective mass through the mass discrepancy. Furthermore, the unattributed peaks at $\sim$27 and 36 cm^{-1} may be related to the crystal structural distortions. Overall, a compress and almost flat phonon dispersion curve is ob-served [Fig. 2(d)], which is clearly signifying the poorer sound propagation and strong crystal anharmonicity in CVS$-$Se$_{30}$S$_2$ than CVS$-$Se$_{32}$. For both compounds, the atomic density of states calculations suggesting that the vibrational properties are highly dominated by the softly bonded CuSe$_4$ tetrahedra.

The acoustic branches are lies below 40 cm^{-1}, further signi-fying the poor thermal properties in these complex structured materials, due to their low acoustic phonon cutoff frequency. We have also calculated the phonon lifetime (τ_i) of the active modes through the obtained full-width half-maxima (FWHM's) via, $\tau_i = \frac{1}{2\pi \text{ FWHM}_i}$, and obtained $\tau_i \leqslant 1$ ps [9]. The short τ_i of Raman active modes suggests the strong phonon scattering.

C. Electrical transport

Temperature dependence of electrical conductivity (σ) decreases with the increase in temperature suggesting the degenerate semiconductor behavior [Fig. 3(a)]. The ordered CVS$-$Se$_{32}$ compound has the lowest σ, whereas, the sulfur doped CVS$-$Se$_{30}$S$_2$ has increased σ. The positive Seebeck coefficient (S) shows that holes are the majority charge car-riers [Fig. 3(b)] and lies in the range of $\sim$50–150 μV K^{-1} for 300–773 K. The electrical transport properties are also verified through the theoretical calculations. The electronic dispersion curve calculations further suggesting similar re-sults as observed experimentally. The extended valance band states above the Fermi level (E_f) [Fig. 3(c) and 3(d)] implies holes are the major charge carriers. Further, the introduc-tion of sulfur dopants enhances the room temperature carrier concentrations from $\sim$3.7 $\times$ 10^{20} cm^{-3} (for CVS$-$Se$_{32}$) to
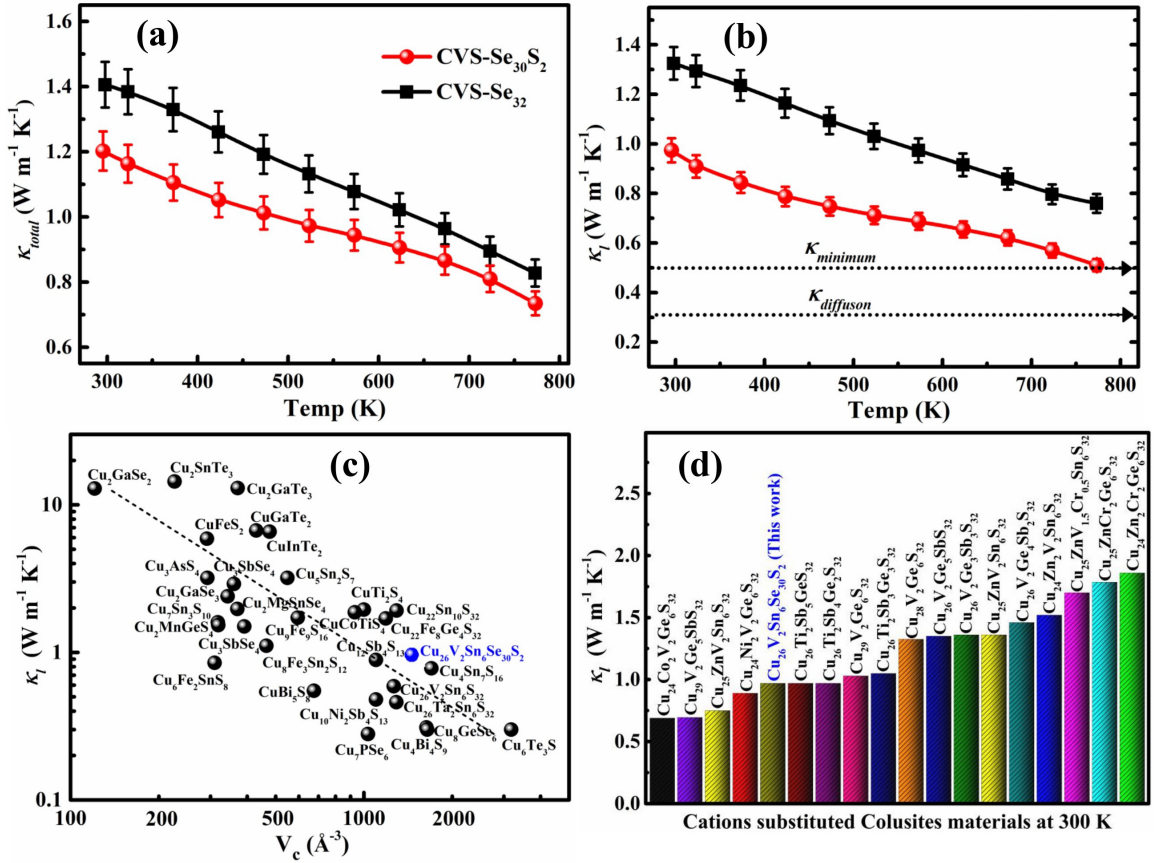
FIG. 4. Temperature-dependent (a) total thermal conductivity (κ_{total}), and (b) lattice thermal conductivity, (κ_l) for CVS$-$Se$_{32}$ and CVS$-$Se$_{30}$S$_2$. (c) The variations of κ_l vs unit cell volume (V_c) in Cu-based complex crystal structure chalcogenides [12,15,36,40–50] and, (d) comparison of room-temperature κ_l for various cation substituted and doped colusites compounds having multiple phonon scattering channels [34,51–55].

$\sim 8.6 \times 10^{20}\,\mathrm{cm}^{-3}$ (for CVS$-$Se$_{30}$S$_2$). The anomalous increase in the Seebeck coefficient for CVS$-$Se$_{30}$S$_2$ even with increase of carrier concentrations is due to flatness in the bands (Fig. S6, SM [35]) observed near the Fermi energy levels, which overall increases the carrier effective mass [37–39]. The inset Fig. 3(c) shows high power factor (PF = σS^2)$\sim 400\,\mu\mathrm{W\,m}^{-1}\,\mathrm{K}^{-2}$ in CVS$-$Se$_{30}$S$_2$, whereas the ordered CVS$-$Se$_{32}$ compound shows low PF $\sim 90\,\mu\mathrm{W\,m}^{-1}\,\mathrm{K}^{-2}$ at ~ 773 K.

D. Thermal transport measurements

Figure 4(a) shows the decreasing κ_{total} for CVS$-$Se$_{32}$, and CVS$-$Se$_{30}$S$_2$ with rise in temperature. The low κ_{total} in these compounds is due to the large number of atoms in the primitive unit cell (N), where N shows inverse dependence with κ_{total}, hence, lower heat transportation [8,12]. At higher temperatures, the amplitude of lattice vibration increases leading to scattering, which further lowers the κ_{total}. The sulfur substitution in the regular crystal framework of CVS$-$Se$_{32}$
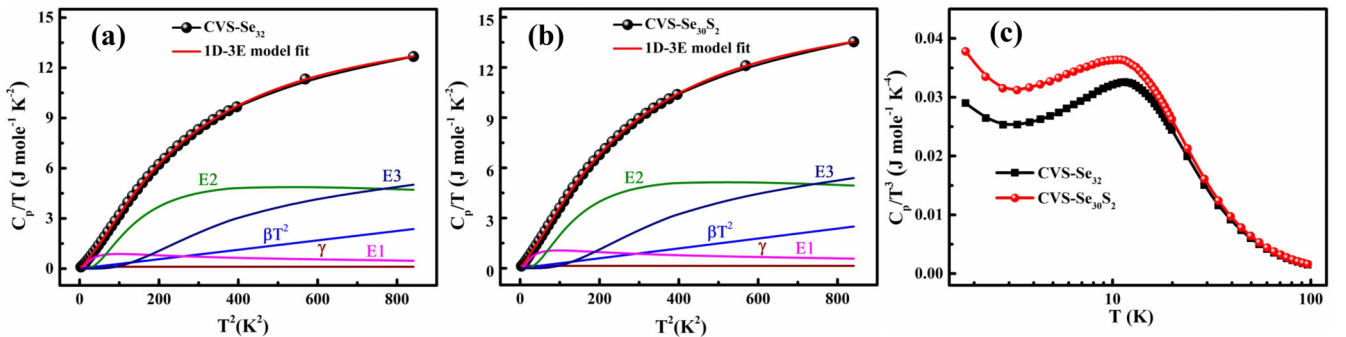

FIG. 5. Temperature dependent C_p for (a) CVS$-$Se$_{32}$, (b) CVS$-$Se$_{30}$S$_2$. The data is best fitted using 1D-3E model due to localized vibrational modes at low-energies, and (c) a hump in the C_p/T^3 vs T plot, shows the presence of disorder and relatively high vibrational density of states in CVS$-$Se$_{30}$S$_2$.
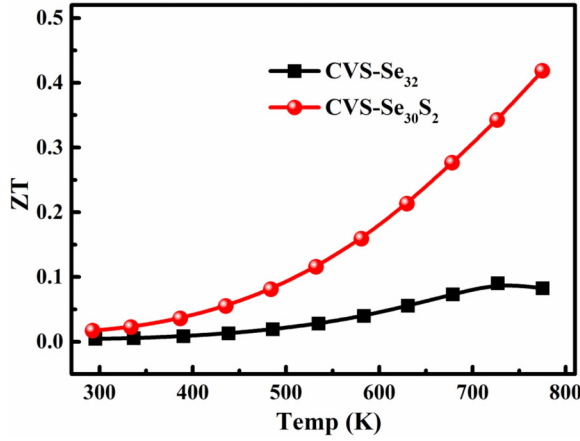
FIG. 6. The TE figure of merit (ZT) for CVS−Se$_{32}$ and CVS−Se$_{30}$S$_2$.

provides the atomic scale disorder and largely disrupts the heat-carrying phonon. Furthermore, the κ_l is calculated by subtracting the electronic thermal conductivity (κ_e) from κ_{total} as, $\kappa_l = \kappa_{total} - \kappa_e$, where the κ_e (Fig. S9) is estimated via the Wiedemann-Franz law, $\kappa_e = \sigma LT$. The Lorenz number (L) (Fig. S10, SM [35]) is calculated by fitting the reduced chemical potential (η), which is derived from the temperature-dependent Seebeck coefficient, single parabolic band, and acoustic phonon scattering [56–58]. The obtained κ_l shows a decreasing trend with increase in temperature [Fig. 4(b)] due to anharmonic umklapp processes (T^{-1} dependence) [59]. At high temperature, the phonon-phonon scattering becomes dominant, creating additional phonon scattering channels, which further lowers to glasslike κ_l value ∼0.51 W m^{-1} K^{-1} (at 773 K) in CVS−Se$_{30}$S$_2$. The experimental observed κ_l is just above the minimum theoretical thermal conductivity ($\kappa_{minimum}$), which is calculated using the Cahill's model for pristine CVS−Se$_{32}$ [60]. The diffusive-mediated thermal conductivity ($\kappa_{diffuson}$) is the lowest possible experimental thermal conductivity for bulk disordered materials related to the average energy of vibrational density of states of a materials and the number density of atoms [61]. The enhanced disorder with S doping in CVS−Se$_{30}$S$_2$ further lowers the κ_l of CVS−Se$_{32}$ to the $\kappa_{minimum}$ level. Recently, a unified theory regarding the minimum and glasslike κ_l is presented for the thermal transport properties of materials [62,63]. The formulation remains accurate for anharmonic, disordered, complex materials with closely spaced and large broadening phonon branches. Furthermore, in general, with increasing the unit cell volume (V_c), the κ_l of the material decreases [5,7,12]. Figure 2(c) shows the inverse relation between κ_l and V_c for various complex structured large unit cell materials. Moreover, Fig. 2(d) shows the comparison of room-temperature κ_l of CVS−Se$_{30}$S$_2$ and various cation substituted and doped colusites materials. The significant low κ_l in CVS−Se$_{30}$S$_2$ indicates the potential towards the thermal applications.

E. Heat capacity analysis

For the detailed analysis about the localized vibrations, disorders, crystal anharmonicity, and acoustic-optical phonon interaction, we have studied and explored the low-temperature

C_p properties [Figs. 5(a) and 5(b)]. Using single Debye model fitting of C_p/T vs T^2, the negative value of electronic heat capacity (γ) term (in the temperature range of ∼1.8–29 K, however, the C_p/T vs T^2 analysis in milli kelvin temperature range might be helpful for more detailed study) (Fig. S11, SM [35]) signify that the C_p analysis can not be examined from single Debye model alone [64]. Therefore, we try to fit the temperature dependence C_p data through Debye and additional localized Einstein modes, as represented by following equation:

$$\frac{C_p}{T} = \gamma + \beta T^2 + \sum_{n=1}^{3}\left(A_n(\Theta_{En})^2\, T^{2\left(-\frac{3}{2}\right)}\frac{e^{\frac{\Theta_{En}}{T}}}{\left(e^{\frac{\Theta_{En}}{T}}-1\right)^2}\right),$$

where first, second, and third term represents the electronic (Sommerfeld), lattice (Debye), and multiple localized oscillators (Einstein) contributions of heat capacity, respectively. Here A_n is the prefactor and Θ_{En} is the Einstein temperature for the nth Einstein oscillators [65]. For CVS−Se$_{32}$ the three characteristic localized Einstein modes positioned at ∼25 (17), 60 (42), and 100 K (70 cm^{-1}), interacts with acoustic and optical modes in the low-frequency regions. For CVS−Se$_{30}$S$_2$, the similar fitting parameters are shown in the Table S1, SM [35]. The large γ (∼0.05–0.2 J mol^{-1} K^{-2}) in complex structured large unit cell compounds has been well observed in earlier reports [9,48,66–69]. The high γ values are originated from the correction term used for multiple Einstein modes (as nonlinearity come into play; factors other than linear term) in addition to the Debye modes [70]. Hence, the deviation in the Debye T^3 law (non-Debye behavior) can be understand by the presence of these excess vibrational density of states. Further, Fig. 5(c) shows a hump at low temperature, known as bosonlike peak, a characteristic peak for materials having high disorder and excess vibrational density of states at low frequency. The significant higher C_p/T^3 shift (high magnitude) of peak value suggests the presence of larger vibrational density of states and more glassy nature in CVS−Se$_{30}$S$_2$ [68].

F. Sound velocity measurements and crystal anharmonicity

The relatively soft vibrations of Cu atoms and rattling-like localized vibrations at low-frequency regime can result in the soft elastic lattice and poor sound velocity. To study in detail, we have estimated the longitudinal (v_l), transverse (v_t), and average (v_m) sound velocities as listed in Table I. The observed v_m∼1998 m sec^{-1} (CVS−Se$_{32}$) and ∼1634 m sec^{-1} (CVS−Se$_{30}$S$_2$) again signify the poor thermal transport properties. The experimental values are well supported by the theoretical results, as evident from the flat vibrational branches (less slope in dispersion curve) and the strong interactions among them. In the large unit cell compounds, the large real space dimensions (lattice parameters) leads to the shrinkage of first Brillouin zone dimensions (in reciprocal space), which results in folding back of high-frequency vibrational modes as compressed and flat optical modes [6]. Hence, the flat optical branches in the dispersion curves carries negligible heat energy, so most of heat energy is carried by the acoustic branches. The poor sound propagation and strong acoustic-optical interaction also lowers the crystal's
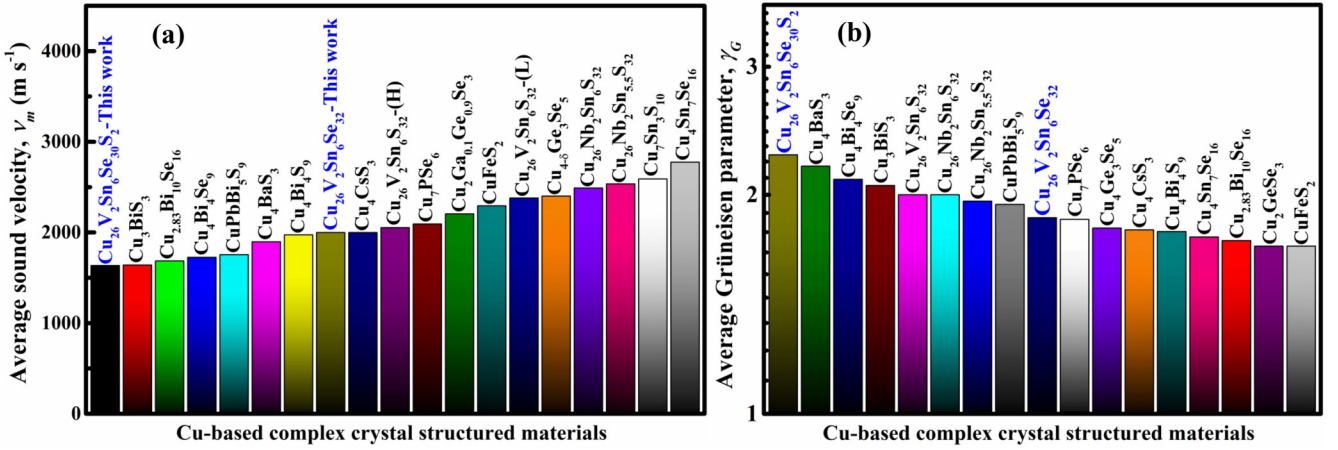
FIG. 7. Comparison of (a) average sound velocity (v_m) and (b) average Grüneisen parameters, (γ_G) of eco-freiendly Cu-based complex structured sulfides and selenides [1,20,22,43,45,49,72–77] The v_m for all these materials is calculated from the reported v_l and be v_t values, by using the formula, $v_m = (\frac{3}{v_l^{-3}+2v_t^{-3}})^{1/3}$, where v_l and be v_t be the longitudinal and transverse sound velocities, respectively. Whereas, average γ_G for all these compounds is calculated through the formula, $\gamma_G = \frac{3}{2}(\frac{1+v_p}{2-3v_p})$, here, v_p is the Poisson ratio of the materials [67].

highest normal mode of vibrations, so the Debye temperature (Θ_D). The obtained Θ_D is lowest than many Cu-based complex structured materials (Fig. S12, SM [35]). We have also quantified the thermodynamically average Grüneisen parameter (γ_G) from the sound velocity measurements, which informs about the presence of crystal anharmonicity and characterize the connection between the crystal volume, phonon frequency, and κ_1. The strong crystal anharmonicity (large γ_G) causes large damping effects, enhances the scattering processes and ultimately lowers the κ_1. The obtained average γ_G are ~1.86 (CVS−Se$_{32}$) and ~2.27 (CVS−Se$_{30}$S$_2$), which is significantly higher than many state-of-the-art TE materials such as Bi$_2$Te$_3$, Sb$_2$Te$_3$ PbTe, PbSe, and PbS [71] Among CVS−Se$_{32}$ and CVS−Se$_{30}$S$_2$, the disorder and mass contrast offered by the substituted sulfur atom in CVS−Se$_{30}$S$_2$ hinders the heat transport effectively through high weighted average Grüneisen parameter and mode Grüneisen parameter for the acoustic modes (Fig. S13, SM [35]). The observed vibrational modes have much lower frequencies for CVS-Se$_{32}$ if compared from Cu$_{26}$Nb$_2$Sn$_6$Se$_{32}$ [9]. The excess vibrational density of states is well driven through localized Einstein

vibrational modes in both V- and Nb-based compounds [9]. Overall, the κ_1 for V-based CVS−Se$_{32}$ is ~1/2 to the Nb-based CNS−Se$_{32}$, throughout the temperature studied region signifying the poor heat transportations [9]. The low acoustic phonon cutoff frequency [Figs. 3(c)–3(d)] also results in poor elastic properties (bulk and shear modulus) due to soft chemical bonding by Cu atoms. Figures S14–S15 (SM [35]) shows the comparison of low bulk and shear modulus for CVS−Se$_{32}$ and CVS−Se$_{30}$S$_2$ than other complex structured compounds, which makes them a potential candidate for poor elastic and thermal transport applications. As the substitution of S in the Se sites results in the enhanced disorder and mass contrast in the crystalline framework. Thus, a relatively higher Poisson's ratio (~0.37) for CVS−Se$_{30}$S$_2$ suggests that it is more prone to lateral deformation under the application of an axial load, which is resulting in significantly smaller shear modulus in comparison with CVS−Se$_{32}$. Furthermore, regarding the TE figure of merit (ZT = $\frac{\sigma S^2}{\kappa_{total}}$ T), ~6% sulfur-doped CVS−Se$_{30}$S$_2$ has ZT~0.42 at 773 K (Fig. 6), which is almost five times higher than CVS−Se$_{32}$.

TABLE I. The longitudinal (v_l), transverse (v_t), and average sound velocities (v_m); minimum ($\kappa_{minimum}$) and diffuson ($\kappa_{diffuson}$) thermal conductivities; Poisson ratio (v_p), Debye temperature (Θ_D), average Grüneisen parameters (γ_G), bulk modulus (B), and shear (G) modulus of complex structured CVS−Se$_{32}$ and CVS−Se$_{30}$S$_2$ materials.

	CVS−Se$_{32}$	CVS−Se$_{30}$S$_2$
Longitudinal sound velocity, v_l (m s^{-1})	~3423	~3150
Transverse sound velocity, v_t (m s^{-1})	~1786	~1450
Average sound velocity, v_m (m s^{-1})	~1998	~1634
Minimum thermal conductivity, $\kappa_{minimum}$ (W m^{-1} K^{-1})	~0.50	~0.43
Diffuson thermal conductivity, $\kappa_{diffuson}$ (W m^{-1} K^{-1})	~0.31	~0.27
Poisson ratio, v_p	~0.31	~0.37
Debye temperature Θ_D, (K)	~212	~174
Average Grüneisen parameters, $\boldsymbol{\gamma_G}$	~1.86	~2.27
Bulk modulus, B (GPa)	~41.0	~38.9
Shear modulus, G (GPa)	~17.5	~11.5

Overall, the weakly bonded Cu atoms in the crystal framework results in poor sound propagation (low v_l and v_t), soft elastic lattice properties, which altogether increases the phonon damping and strongly hinders the phonons transportations. The presence of disorders at the anionic sites of $CVS-Se_{30}S_2$ leads to low v_m and high average γ_G values [Figs. 7(a) and 7(b)], which make it a poor thermal conductive material than many Cu-based large unit cells, complex structured, and ecofriendly sulfides and selenides.

IV. SUMMARY

In summary, the large number of atoms in the unit cell can bring the different energy scaled acoustic and optical phonon branches together. The strong interaction between the branches hinders the heat-carrying phonon's momentum strongly by virtue of which the κ_1 of the materials can be tuned. The poor sound propagation, large Grüneisen parameter and weakly bonded Cu atoms altogether reveals about the strong acoustic-optical phonon interactions and poor thermal properties in the complex structured large unit cell materials. The flat dispersion curves for optical branches further signify that most of the heat is carried by the acoustic branches. The presence of several low-frequency optical modes is originated from the soft bonded Cu atom vibrations. Further, the presence of structural disorder and excess localized vibrational density of states leads deviation in the Debye T^3 law. The tailoring of sulfur atom in selenium sites affects both electrical and thermal transport properties, significantly. Overall, due to ultralow $\kappa_1 \sim 0.5\,\mathrm{W\,m^{-1}\,K^{-1}}$ in $CVS-Se_{30}S_2$, the copper-based complex structured material can be considered as a potential candidate for future energy harvesting applications.

[1] G. Guélou, P. Lemoine, B. Raveau, and E. Guilmeau, Recent developments in high-performance thermoelectric sulphides: An overview of the promising synthetic colusites, J. Mater. Chem. C **9**, 773 (2021).

[2] K. Suekuni and T. Takabatake, Cu–S based synthetic minerals as efficient thermoelectric materials at medium temperatures, APL Mater. **4**, 104503 (2016).

[3] A. V. Powell, Recent developments in Earth-abundant copper-sulfide thermoelectric materials, J. Appl. Phys. **126**, 100901 (2019).

[4] P. Qiu, X. Shi, and L. Chen, Cu-based thermoelectric materials, Energy Storage Mater. **3**, 85 (2016).

[5] K. S. Rana and A. Soni, Thermoelectricity in Ag/Cu-based complex crystal structure minerals with inherent low thermal conductivity, Oxford Open Materials Science **3**, itad005 (2023).

[6] Z. Chen, X. Zhang, and Y. Pei, Manipulation of phonon transport in thermoelectrics, Adv. Mater. **30**, 1705617 (2018).

[7] W. Kim, Strategies for engineering phonon transport in thermoelectrics, J. Mater. Chem. C **3**, 10336 (2015).

[8] S. Lin, W. Li, and Y. Pei, Thermally insulative thermoelectric argyrodites, Mater. Today **48**, 198 (2021).

[9] K. S. Rana, R. Gupta, D. Sarkar, N. K. Singh, S. Acharya, S. Vitta, C. Bera, K. Biswas, and A. Soni, Interaction of acoustic and optical phonons in a soft-bonded Cu-Se framework of large unit cell minerals with anionic disorders, Phys. Rev. B **108**, 045202 (2023).

[10] A. Bhui, M. Dutta, M. Mukherjee, K. S. Rana, A. K. Singh, A. Soni, and K. Biswas, Ultralow thermal conductivity in earth-abundant $Cu_{1.6}Bi_{4.8}S_8$: anharmonic rattling of interstitial Cu, Chem. Mater. **33**, 2993 (2021).

[11] C. Bourgès, Y. Bouyrie, A. R. Supka, R. Al Rahal Al Orabi, P. Lemoine, O. I. Lebedev, M. Ohta, K. Suekuni, V. Nassif, V. Hardy *et al.*, High-Performance thermoelectric bulk colusite by process controlled structural disordering, J. Am. Chem. Soc. **140**, 2186 (2018).

[12] K. Suekuni, Y. Shimizu, E. Nishibori, H. Kasai, H. Saito, D. Yoshimoto, K. Hashikuni, Y. Bouyrie, R. Chetty, M. Ohta *et al.*, Atomic-scale phonon scatterers in thermoelectric colusites with a tetrahedral framework structure, J. Mater. Chem. A **7**, 228 (2019).

[13] K. Suekuni, F. S. Kim, H. Nishiate, M. Ohta, H. I. Tanaka, and T. Takabatake, High-performance thermoelectric minerals: Colusites $Cu_{26}V_2M_6S_{32}$ (M = Ge, Sn), Appl. Phys. Lett. **105**, 132107 (2014).

[14] Y. Bouyrie, C. Candolfi, S. Pailhès, M. M. Koza, B. Malaman, A. Dauscher, J. Tobola, O. Boisron, L. Saviot, and B. Lenoir, From crystal to glass-like thermal conductivity in crystalline minerals, Phys. Chem. Chem. Phys. **17**, 19751 (2015).

[15] K. Suekuni, K. Tsuruta, M. Kunii, H. Nishiate, E. Nishibori, S. Maki, M. Ohta, A. Yamamoto, and M. Koyano, High-performance thermoelectric mineral $Cu_{12-x}Ni_xSb_4S_{13}$ tetrahedrite, J. Appl. Phys. **113**, 043712 (2013).

[16] T. Plirdpring, K. Kurosaki, A. Kosuga, T. Day, S. Firdosy, V. Ravi, G. J. Snyder, A. Harnwunggmoung, T. Sugahara, Y. Ohishi *et al.*, Chalcopyrite $CuGaTe_2$: A high-efficiency bulk thermoelectric material, Adv. Mater. **24**, 3622 (2012).

[17] P. Qiu, T. Zhang, Y. Qiu, X. Shi, and L. Chen, Sulfide bornite thermoelectric material: A natural mineral with ultralow thermal conductivity, Energy Environ. Sci. **7**, 4000 (2014).

[18] Y. Yang, P. Ying, J. Wang, X. Liu, Z. Du, Y. Chao, and J. Cui, Enhancing the thermoelectric performance of Cu_3SnS_4-based solid solutions through coordination of the Seebeck coefficient and carrier concentration, J. Mater. Chem. A **5**, 18808 (2017).

[19] J. M. Skelton, A. J. Jackson, M. Dimitrievska, S. K. Wallace, and A. Walsh, Vibrational spectra and lattice thermal conductivity of kesterite-structured Cu_2ZnSnS_4 and $Cu_2ZnSnSe_4$, APL Mater. **3**, 041102 (2015).

[20] F. Jia, S. Zhao, J. Wu, L. Chen, T.-H. Liu, and L.-M. Wu, Cu_3BiS_3: two-dimensional coordination induces out-of-plane phonon scattering enabling ultralow thermal conductivity, Angew. Chem. Int. Ed. **62**, e202315642 (2023).

[21] W. Lai, Y. Wang, D. T. Morelli, and X. Lu, From bonding asymmetry to anharmonic rattling in $Cu_{12}Sb_4S_{13}$ tetrahedrites: when lone-pair electrons are not so lonely, Adv. Funct. Mater. **25**, 3648 (2015).

[22] N. Ma, F. Li, J.-G. Li, X. Liu, D.-B. Zhang, Y.-Y. Li, L. Chen, and L.-M. Wu, Mixed-valence $CsCu_4Se_3$: large phonon anharmonicity driven by the hierarchy of the rigid $[(Cu^+)_4(Se^{2-})_2](Se^-)$ double anti$-CaF_2$ layer and the soft Cs^+ sublattice, J. Am. Chem. Soc. **143**, 18490 (2021).

[23] F. S. Kim, K. Suekuni, H. Nishiate, M. Ohta, H. I. Tanaka, and T. Takabatake, Tuning the charge carrier density in the thermoelectric colusite, J. Appl. Phys. **119**, 175105 (2016).

[24] Y. Bouyrie, M. Ohta, K. Suekuni, Y. Kikuchi, P. Jood, A. Yamamoto, and T. Takabatake, Enhancement in the thermoelectric performance of colusites $Cu_{26}A_2E_6S_{32}$ (A = Nb, Ta; E = Sn, Ge) using E-site non-stoichiometry, J. Mater. Chem. C **5**, 4174 (2017).

[25] P. Masschelein, C. Candolfi, A. Dauscher, C. Gendarme, A. R. A. O. Rabih, P. Gougeon, M. Potel, P. Gall, R. Gautier, and B. Lenoir, Influence of S and Te substitutions on the thermoelectric properties of the cluster compound $Ag_{3.8}Mo_9Se_{11}$, J. Alloys Compd. **739**, 360 (2018).

[26] T. Zhang, X. Su, Y. Yan, W. Liu, Y. You, H. Xie, D. Yang, C. Uher, and X. Tang, Structure and thermoelectric properties of 2D $Cr_2Se_{3-3x}S_{3x}$ solid solutions, J. Mater. Chem. C **6**, 836 (2018).

[27] P. Jood and M. Ohta, Effect of sulfur substitution on the thermoelectric properties of $(SnSe)_{1.16}NbSe_2$: Charge transfer in a misfit layered structure, RSC Adv. **6**, 105653 (2016).

[28] P. E. Blöchl, Projector augmented-wave method, Phys. Rev. B **50**, 17953 (1994).

[29] G. Kresse and J. Furthmüller, Efficient iterative schemes for ab initio total-energy calculations using a plane-wave basis set, Phys. Rev. B **54**, 11169 (1996).

[30] G. Kresse and D. Joubert, From ultrasoft pseudopotentials to the projector augmented-wave method, Phys. Rev. B **59**, 1758 (1999).

[31] J. P. Perdew, K. Burke, and M. Ernzerhof, Generalized gradient approximation made simple, Phys. Rev. Lett. **77**, 3865 (1996).

[32] A. Togo and I. Tanaka, First principles phonon calculations in materials science, Scr. Mater. **108**, 1 (2015).

[33] G. Guélou, V. Pavan Kumar, A. Bourhim, P. Lemoine, B. Raveau, A. Supka, O. I. Lebedev, R. Al Rahal Al Orabi, M. Fornari, K. Suekuni et al., Toppling the transport properties with cationic overstoichiometry in thermoelectric colusite: $[Cu_{26}Cr_2Ge_6]_{1+\delta}S_{32}$, Appl. Energy Mater. **3**, 4180 (2020).

[34] Y. Shimizu, K. Suekuni, H. Saito, P. Lemoine, E. Guilmeau, B. Raveau, R. Chetty, M. Ohta, T. Takabatake, and M. Ohtaki, Synergistic effect of chemical substitution and insertion on the thermoelectric performance of $Cu_{26}V_2Ge_6S_{32}$ colusite, Inorg. Chem. **60**, 11364 (2021).

[35] See Supplemental Material at http://link.aps.org/supplemental/10.1103/PhysRevB.109.115202 for structural, electrical and thermal transport properties.

[36] Y. Kikuchi, Y. Bouyrie, M. Ohta, K. Suekuni, M. Aihara, and T. Takabatake, Vanadium-free colusites $Cu_{26}A_2Sn_6S_{32}$ (A = Nb, Ta) for environmentally friendly thermoelectrics, J. Mater. Chem. A **4**, 15207 (2016).

[37] S. Li, Z. Tong, and H. Bao, Resolving different scattering effects on the thermal and electrical transport in doped SnSe, J. Appl. Phys. **126**, 025111 (2019).

[38] H. Namiki, M. Kobayashi, K. Nagata, Y. Saito, N. Tachibana, and Y. Ota, Relationship between the density of states effective mass and carrier concentration of thermoelectric phosphide $Ag_6Ge_{10}P_{12}$ with strong mechanical robustness, Mater. Today Sustain. **18**, 100116 (2022).

[39] E. Isotta, B. Mukherjee, C. Fanciulli, N. Ataollahi, I. Sergueev, S. Stankov, R. Edla, N. M. Pugno, and P. Scardi, Origin of a simultaneous suppression of thermal conductivity and increase of electrical conductivity and seebeck coefficient in disordered cubic Cu_2ZnSnS_4, Phys. Rev. Appl. **14**, 064073 (2020).

[40] Z. Liu, W. Zhang, W. Gao, and T. Mori, A material catalogue with glass-like thermal conductivity mediated by crystallographic occupancy for thermoelectric application, Energy Environ. Sci. **14**, 3579 (2021).

[41] C. Bourgès, V. Pavan Kumar, H. Nagai, Y. Miyazaki, B. Raveau, and E. Guilmeau, Role of cobalt for titanium substitution on the thermoelectric properties of the thiospinel $CuTi_2S_4$, J. Alloys Compd. **781**, 1169 (2019).

[42] V. Pavan Kumar, S. Passuti, B. Zhang, S. Fujii, K. Yoshizawa, P. Boullay, S. Le Tonquesse, C. Prestipino, B. Raveau, P. Lemoine et al., Engineering transport properties in interconnected enargite-stannite type $Cu_{2+x}Mn_{1-x}GeS_4$ nanocomposites, Angew. Chem. Int. Ed. **61**, e202210600 (2022).

[43] T. Deng, T.-R. Wei, Q. Song, Q. Xu, D. Ren, P. Qiu, X. Shi, and L. Chen, Thermoelectric properties of n-type $Cu_4Sn_7S_{16}-$based compounds, RSC Adv. **9**, 7826 (2019).

[44] V. P. Kumar, P. Lemoine, V. Carnevali, G. Guélou, O. I. Lebedev, B. Raveau, R. Al Rahal Al Orabi, M. Fornari, C. Candolfi, C. Prestipino et al., Local-Disorder-Induced low thermal conductivity in degenerate semiconductor $Cu_{22}Sn_{10}S_{32}$, Inorg. Chem. **60**, 16273 (2021).

[45] T. Deng, T. Xing, M. Brod, Y. Sheng, P. Qiu, I. Veremchuk, Q. Song, T.-R. Wei, J. Yang, G. Snyder et al., Discovery of high-performance thermoelectric copper chalcogenide using modified diffusion-couple high-throughput synthesis and automated histogram analysis technique, Energy Environ. Sci. **13**, 3041 (2020).

[46] L. Paradis Fortin, G. Guélou, P. Ventrapati, P. Lemoine, C. Prestipino, O. Merdrignac-Conanec, G. R. Durand, S. Cordier, and O. Lebedev, Structure, microstructure and thermoelectric properties of germanite-type $Cu_{22}Fe_8Ge_4S_{32}$ compounds, J. Alloys Compd. **831**, 154767 (2020).

[47] I. Siloi, P. Gopal, S. Curtarolo, M. B. Nardelli, P. Vaqueiro, and M. Fornari, Thermoelectric properties of minerals with the mawsonite structure, ACS Appl. Energy Mater. **2**, 8068 (2019).

[48] B. Jiang, P. Qiu, E. Eikeland, H. Chen, Q. Song, D. Ren, T. Zhang, J. Yang, B. B. Iversen, X. Shi et al., Cu_8GeSe_6-based thermoelectric materials with an argyrodite structure, J. Mater. Chem. C **5**, 943 (2017).

[49] K. S. Weldert, W. G. Zeier, T. W. Day, M. Panthöfer, G. J. Snyder, and W. Tremel, Thermoelectric transport in Cu_7PSe_6 with high copper ionic mobility, J. Am. Chem. Soc. **136**, 12035 (2014).

[50] C. Zhu, H. Ming, L. Huang, B. Zhang, X. Lou, D. Li, B. Jabar, H. Xin, J. Zhang, and X. Qin, Achieving high power factor and thermoelectric performance through dual substitution of Zn and

Se in tetrahedrites $Cu_{12}Sb_4S_{13}$, Appl. Phys. Lett. **115**, 182102 (2019).

[51] Y. Bouyrie, V. Ohorodniichuk, S. Sassi, P. Masschelein, A. Dauscher, C. Candolfi, and B. Lenoir, High-Temperature transport properties of colusite $Cu_{24}T_2V_2Ge_6S_{32}$ (T = Ni, Co), J. Electron. Mater. **46**, 2684 (2016).

[52] T. Hagiwara, K. Suekuni, P. Lemoine, A. R. Supka, R. Chetty, E. Guilmeau, B. Raveau, M. Fornari, M. Ohta, R. Al Rahal Al Orabi *et al.*, Key role of d^0 and d^{10} cations for the design of semiconducting colusites: large thermoelectric ZT in $Cu_{26}Ti_2Sb_6S_{32}$ compounds, Chem. Mater. **33**, 3449 (2021).

[53] P. Kamińska, C. Bourgès, R. Chetty, D. Gutiérrez-Del-Río, P. Śpiewak, W. Święszkowski, T. Nishimura, and T. Mori, Insight into the preponderant role of the lattice size in Sn-based colusites for promoting a high power factor, J. Mater. Chem. A **10**, 10701 (2022).

[54] C. Bourgès, M. Gilmas, P. Lemoine, N. E. Mordvinova, O. I. Lebedev, E. Hug, V. Nassif, B. Malaman, R. Daou, and E. Guilmeau, Structural analysis and thermoelectric properties of mechanically alloyed colusites, J. Mater. Chem. C **4**, 7455 (2016).

[55] V. Pavan Kumar, S. Mitra, G. Guélou, A. R. Supka, P. Lemoine, B. Raveau, R. Al Rahal Al Orabi, M. Fornari, K. Suekuni, and E. Guilmeau, Transport properties and electronic density-of-states of Zn-doped colusite $Cu_{26}Cr_2Ge_6S_{32}$, Appl. Phys. Lett. **117**, 173902 (2020).

[56] H.-S. Kim, Z. M. Gibbs, Y. Tang, H. Wang, and G. J. Snyder, Characterization of Lorenz number with Seebeck coefficient measurement, APL Mater. **3**, 041506 (2015).

[57] Q. Zhang, B. Liao, Y. Lan, K. Lukas, W. Liu, K. Esfarjani, C. Opeil, D. Broido, G. Chen, and Z. Ren, High thermoelectric performance by resonant dopant indium in nanostructured SnTe, Proc. Natl. Acad. Sci. USA **110**, 13261 (2013).

[58] K. Biswas, J. He, I. D. Blum, C.-I. Wu, T. P. Hogan, D. N. Seidman, V. P. Dravid, and M. G. Kanatzidis, High-performance bulk thermoelectrics with all-scale hierarchical architectures, Nature (London) **489**, 414 (2012).

[59] B. Abeles, Lattice thermal conductivity of disordered semiconductor alloys at high temperatures, Phys. Rev. **131**, 1906 (1963).

[60] D. G. Cahill, S. K. Watson, and R. O. Pohl, Lower limit to the thermal conductivity of disordered crystals, Phys. Rev. B **46**, 6131 (1992).

[61] M. T. Agne, R. Hanus, and G. J. Snyder, Minimum thermal conductivity in the context of diffuson-mediated thermal transport, Energy Environ. Sci. **11**, 609 (2018).

[62] M. Simoncelli, N. Marzari, and F. Mauri, Unified theory of thermal transport in crystals and glasses, Nat. Phys. **15**, 809 (2019).

[63] Y. Xia, D. Gaines, J. He, K. Pal, Z. Li, M. G. Kanatzidis, V. Ozoliņš, and C. Wolverton, A unified understanding of minimum lattice thermal conductivity, Proc. Natl. Acad. Sci. **120**, e2302541120 (2023).

[64] A. Sussardi, T. Tanaka, A. U. Khan, L. Schlapbach, and T. Mori, Enhanced thermoelectric properties of samarium boride, J. Materiomics **1**, 196 (2015).

[65] I. K. Dimitrov, M. E. Manley, S. M. Shapiro, J. Yang, W. Zhang, L. D. Chen, Q. Jie, G. Ehlers, A. Podlesnyak, J. Camacho *et al.*, Einstein modes in the phonon density of states of the single-filled skutterudite $Yb_{0.2}Co_4Sb_{12}$, Phys. Rev. B **82**, 174301 (2010).

[66] S. Acharya, J. Pandey, and A. Soni, Enhancement of power factor for inherently poor thermal conductor Ag_8GeSe_6 by replacing Ge with Sn, ACS Appl. Energy Mater. **2**, 654 (2019).

[67] P. Acharyya, T. Ghosh, K. Pal, K. S. Rana, M. Dutta, D. Swain, M. Etter, A. Soni, U. V. Waghmare, and K. Biswas, Glassy thermal conductivity in $Cs_3Bi_2I_6Cl_3$ single crystal, Nature Commun. **13**, 5053 (2022).

[68] C. Candolfi, G. Guélou, C. Bourgès, A. R. Supka, R. Al Rahal Al Orabi, M. Fornari, B. Malaman, G. Le Caër, P. Lemoine, V. Hardy *et al.*, Disorder-driven glasslike thermal conductivity in colusite $Cu_{26}V_2Sn_6S_{32}$ investigated by Mössbauer spectroscopy and inelastic neutron scattering, Phys. Rev. Mater. **4**, 025404 (2020).

[69] E. Lara-Curzio, A. F. May, O. Delaire, M. A. McGuire, X. Lu, C.-Y. Liu, E. D. Case, and D. T. Morelli, Low-temperature heat capacity and localized vibrational modes in natural and synthetic tetrahedrites, J. Appl. Phys. **115**, 193515 (2014).

[70] H. Xie, S. Hao, J. Bao, T. J. Slade, G. J. Snyder, C. Wolverton, and M. G. Kanatzidis, All-Inorganic halide perovskites as potential thermoelectric materials: dynamic cation off-centering induces ultralow thermal conductivity, J. Am. Chem. Soc. **142**, 9553 (2020).

[71] T. Jia, G. Chen, and Y. Zhang, Lattice thermal conductivity evaluated using elastic properties, Phys. Rev. B **95**, 155206 (2017).

[72] Y. Jiang, F. Jia, L. Chen, and L.-M. Wu, $Cu_4Bi_4Se_9$: A thermoelectric symphony of rattling, anharmonic lone-pair, and structural complexity, ACS Appl. Mater. Interfaces **11**, 36616 (2019).

[73] K. Maji, P. Lemoine, A. Renaud, B. Zhang, X. Zhou, V. Carnevali, C. Candolfi, B. Raveau, R. Al Rahal Al Orabi, M. Fornari *et al.*, A tunable structural family with ultralow thermal conductivity: copper-deficient $Cu_{1-x}\square_xPb_{1-x}Bi_{1+x}S_3$, J. Am. Chem. Soc. **144**, 1846 (2022).

[74] Z. Ye, W. Peng, F. Wang, A. Balodhi, R. Basnet, J. Hu, A. Zevalkink, and J. Wang, Quasi-layered crystal structure coupled with point defects leading to ultralow lattice thermal conductivity in n-type $Cu_{2.83}Bi_{10}Se_{16}$, ACS Appl. Energy Mater. **4**, 11325 (2021).

[75] B. Shan, S. Lin, Z. Bu, J. Tang, Z. Chen, X. Zhang, W. Li, and Y. Pei, Thermoelectric properties of $Cu_4Ge_3Se_5$ with an intrinsic disordered zinc blende structure, J. Mater. Chem. A **8**, 3431 (2020).

[76] J. Y. Cho, X. Shi, J. R. Salvador, G. P. Meisner, J. Yang, H. Wang, A. A. Wereszczak, X. Zhou, and C. Uher, Thermoelectric properties and investigations of low thermal conductivity in Ga-doped Cu_2GeSe_3, Phys. Rev. B **84**, 085207 (2011).

[77] P.-a. Zong, K. Kimata, Z. Li, P. Zhang, J. Liang, C. Wan, and K. Koumoto, A p-type thermoelectric material $BaCu4S_3$ with high electronic band degeneracy, J. Appl. Phys. **126**, 025102 (2019).